PROCEEDINGS OF SPIE

SPIEDigitalLibrary.org/conference-proceedings-of-spie

Robust, regularized wavefront reconstruction of Shack-Hartmann data in discontinuous flow

Zareb Noel, Matthew Kemnetz, Stanislav Gordeyev, R. Mark Rennie

Zareb A. Noel, Matthew R. Kemnetz, Stanislav Gordeyev, R. Mark Rennie, "Robust, regularized wavefront reconstruction of Shack-Hartmann data in discontinuous flow," Proc. SPIE 12693, Unconventional Imaging, Sensing, and Adaptive Optics 2023, 1269318 (4 October 2023); doi: 10.1117/12.2677884

SPIE.

Event: SPIE Optical Engineering + Applications, 2023, San Diego, California, United States

Robust, regularized wavefront reconstruction of Shack-Hartmann data in discontinuous flow

Zareb A. Noel[a], Matthew R. Kemnetz[b], Stanislav Gordeyev[a], and R. Mark Rennie[a]

[a]Institute for Flow Physics and Control (FlowPAC) , Hessert Laboratory for Aerospace Research, University of Notre Dame, Notre Dame, Indiana, 46556
[b]Air Force Research Laboratory, Kirtland Air Force Base, New Mexico, 87117

ABSTRACT

Current Shack-Hartmann Wavefront Sensor (SHWFS) reconstruction algorithms for aero-optical research underperform in the presence of flow features with strong density gradients, such as shockwaves in supersonic flow. The large density variations in shockwaves violate the key underlying assumption of SHWFS; that local changes in the wavefront within the lenslet subaperture manifest primarily as tip/tilt. In these cases, the image-plane irradiance pattern of individual lenslets can exhibit high-order aberrations, resulting in non-tip/tilt behaviors. Standard least-squares wavefront reconstruction methods fail to accurately recover the wavefront in the presence of a shock due to the least-squares estimator's tendency to give too much "influence" to outliers present in the measured SHWFS data, resulting in an underprediction of the optical-path difference (OPD) across the shock. A new algorithm is described to overcome the limitations of the standard least-squares reconstruction method. Two weighting functions are investigated with the aim of using additional intensity information to quantify the degree to which each subaperture is aberrated. The least-squares estimator is replaced with a robust estimator to perform outlier handling and regularizing terms are then used to further constrain the spatial organization of the solution. The problem of wavefront reconstruction is cast as a global functional optimization problem where minimization is achieved iteratively. The algorithm is then evaluated on a sample of Mach 6 SHWFS dot patterns where oblique shocks produce flow discontinuities. The results show that the algorithm is capable of accurately targeting discontinuous flow features as outliers, and subsequently altering those outliers, increasing the OPD as well as the sharpness of the shockwave structure.

Keywords: Manuscript format, template, SPIE Proceedings, LaTeX

1. INTRODUCTION

For turbulent, compressible flow, spatiotemporal variations in the local density lead to commensurate variations in the local index of refraction.[1] While this "aero-optical" effect can be exploited to measure the fluid-mechanical behavior of a variable-density flow, it presents considerable challenges when the objective is to propagate light *through* variable density fluids while maintaining phase coherence, such as in airborne optical communication. It is no surprise then, that measuring and compensating for aero-optical effects is of prime importance when designing airborne optical systems operating in compressible flow conditions.

Index of refraction variations in the beam are related to density variations via the Gladstone-Dale relationship:

$$n = 1 + K_{GD}\rho, \tag{1}$$

Further author information: (Send correspondence to Z.A. Noel)
Z.A. Noel: znoel@nd.edu
M.R. Kemnetz: matthew.kemnetz@us.af.mil
S. Gordeyev: sgordeye@nd.edu
R.M. Rennie: rrennie@nd.edu

Unconventional Imaging, Sensing, and Adaptive Optics 2023, edited by Jean J. Dolne, Mark F. Spencer, Santasri R. Bose-Pillai, Proc. of SPIE Vol. 12693, 1269318
 · 0277-786X · doi: 10.1117/12.2677884

where the density, ρ is related to the index of refraction, n, through the Gladstone-Dale constant, K_{GD}.The optical path difference (OPD) is then the integrated effect of the mean-removed index of refraction variations along the beam path,

$$OPD(x,y) = \int \rho'(x,y,z)dz, \tag{2}$$

where ρ' indicates fluctuations in the density and propagation in the z direction is assumed. The OPD distortions negatively impact the ability of airborne optics systems to focus their optical power onto a target. Typical methods of mitigating beam distortions usually include using adaptive optics compensation systems that correct wavefront aberrations.[2] Additionally, flow control strategies may be employed to improve the aero-optical environment that a laser is propagating through.[3] The performance of these methods is dependent on the accuracy of wavefront measurement and reconstruction. The most common method for measuring aero-optical wavefronts is the Shack-Hartmann Wavefront Sensor (SHWFS), which has the advantage of being cost-effective and relatively easy to deploy. The SHWFS partitions the beam using an array of lenslets that focus the light onto the image plane of a detector, as shown in Fig.1 allowing representation of the wavefront as an array of local tilt measurements. While not an issue in many cases, the large density gradients associated with flow phenomena such as deep turbulence,[4,5] highly vortical flow,[6] and shockwaves[7,8] cause high -order aberrations in the focused SHWFS dot pattern that limit the accuracy of SHWFS measurements. As aerospace technology advances—especially regarding light propagation through variable density flows—demands on the capabilities of these measurement techniques also increase. As such, the purpose of this research is to overcome the limitations of the SHWFS measurements by recovering more accurate wavefront estimations from data acquired in the presence of shocks, deep turbulence and similar environments.

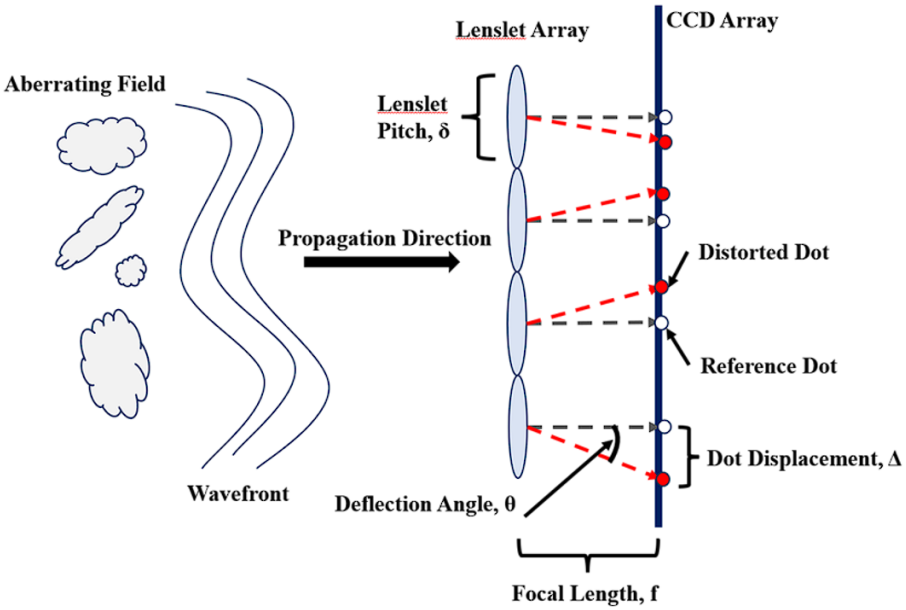

Figure 1. An example diagram of the SHWFS measurement system.

Consider the standard method of processing SHWFS dot patterns; the first central moment of each dot is computed as,

$$\overline{x} = \frac{\iint I(x,y)xdxdy}{\iint I(x,y)dxdy}, \tag{3}$$

where $I(x,y)$ is the recorded intensity within the lenslet area-of-interest (AOI), and x is the spatial location (similar equation for y direction). Absent any extreme flow phenomena as previously mentioned, Equation (1)

provides an accurate result for the focused dot position. Dot positions (centroids) are then used to obtain the local wavefront gradient,

$$\theta = \frac{(x - \overline{x})}{f_L}, \tag{4}$$

where θ is the measurement of the local wavefront gradient at each AOI and f_L is the focal length of the lenslet. Now consider imaging through a shockwave, as in Kalensky et al.;[8] strong density variations cause the dot to bifurcate, fundamentally changing the nature of the subaperture intensity distribution. This dot bifurcation violates the underlying premise of the SHWFS measurement technique; that the local wavefront slope for a given lenslet is solely optical tip/tilt. While the focus of this current research is on recovering more accurate wavefront estimations from aero-optical data such as shockwaves, another example of this problem can be seen in works investigating the impact of deep turbulence on SHWFS measurements.[9] Here, the accumulation of density fluctuations in the optical path causes destructive interference in the propagating laser, resulting in significant intensity fluctuations and beam spreading in the image plane, called scintillation. As will be discussed in more detail, these violations can be regarded as outliers in the data that can be handled in a statistical fashion.

2. OUTLIER DETECTION IN SHWFS

2.1 Least-Squares Wavefront Reconstruction

In standard reconstruction algorithms, slope measurements from the SHWFS are used to reconstruct the wavefront by minimizing the difference between the gradient of the reconstructed wavefront and the measured slopes at each point in the image domain. This may be expressed as a global energy minimization problem,

$$J(W) = \iint \|\nabla W - \theta\|_2^2 dxdy, \tag{5}$$

where ∇W is the gradient of the wavefront estimation, θ is the measured slopes and $J(W)$ is the global energy functional to be minimized. Standard reconstruction algorithms solve this linear least-squares problem using a sparse matrix approach, which is a relatively inexpensive computation that can be done by solving the normal equations, see.[10–12] For continuous representations of this problem, optimality conditions may be obtained using the Euler-Lagrange Method, which results in the strong formulation of Equation (5),

$$\frac{\partial^2 W}{\partial x^2} + \frac{\partial^2 W}{\partial y^2} = \frac{\partial \theta_x}{\partial x} + \frac{\partial \theta_y}{\partial y}, \tag{6}$$

where Equation (6) is a Poisson's Equation, constraining the divergence of the slope to match the Laplacian of the reconstructed wavefront at every spatial point in the domain.

Unlike solutions to other inverse problems, where the outliers are readily identifiable within the data,[13] outliers in SHWFS are expressed in a different way. There are two main classes of outliers discussed in this work: data outliers and spatial outliers. Data outliers constitute violations of the underlying assumptions present within SHWFS measurements, stemming from limitations of the measurment system itself. Spatial outliers indicate violations in the physical assumptions imposed on the spatial organization or "coherence" of the solution.

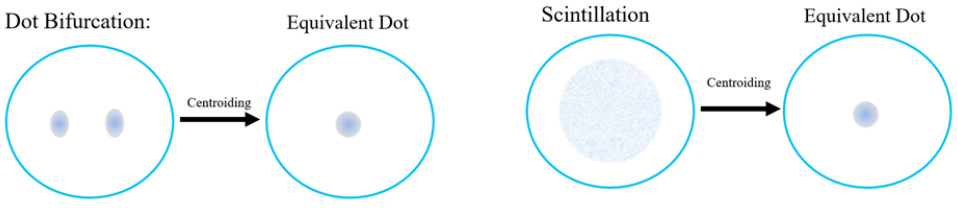

Figure 2. Schematic of AOI with dot bifurcation (left) and scintillation (right). Taking the centroid of both cases yields a centroid equivalent to one from a dot that does not violate the tip/tilt measurement assumption of SHWFS.

For data outliers, consider typical violations of the assumptions inherent in SHWFS measurements such as: dot bifurcation due to a shockwave or scintillation due to extreme atmospheric turbulence. Recall Equation (4); the slope measurements are dependent on the calculated centroids within a lenslet AOI. Consider the example of Fig.2, for both dot bifurcation and dot scintillation. Centroids calculated using Equation (3) would certainly yield a value for the centroid. Even in the case of total intensity dropout due to the existence of a branch point, the reference centroid would be used, essentially returning a value of 0 for the local wavefront gradient. It is therefore straightforward to conclude that, in the case of data outliers due to non-tilt behavior in the lenslet array, the centroid calculated is not representative of the true local wavefront gradient at that measurement location. Put another way; the standard method of wavefront reconstruction from SHWFS measurements is *blind* to the true magnitude of the local wavefront gradient, and therefore its own data outliers. In fact, the local wavefront gradient should be higher than what the SHWFS would typically indicate. For example, in Kalensky et al.,[8] it is noted that, for changes in OPD greater than 0.5π rad, standard least-squares reconstruction leads to a significant underestimation of the wavefront value across the shock.

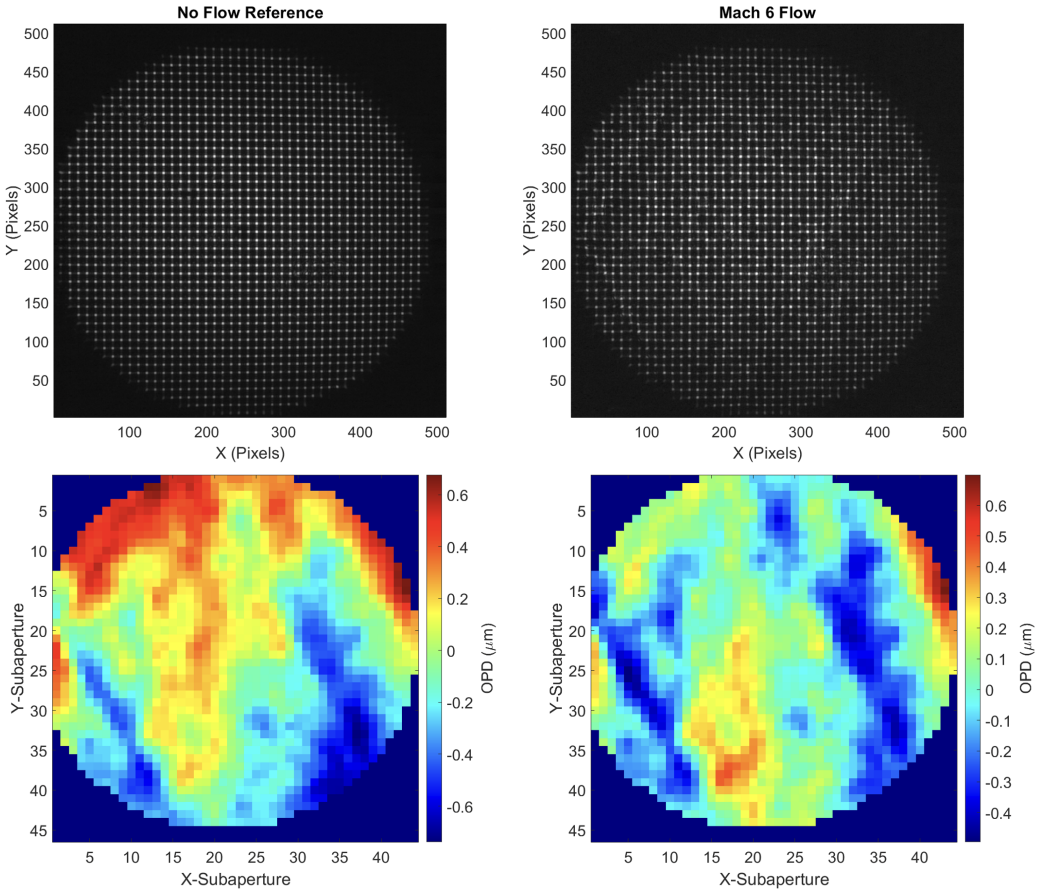

Figure 3. Raw SHWFS dot patterns showing no-flow reference (top left) and Mach 6 flow (top right). Least-squares reconstruction without tip/tilt/piston removal (bottom left) and with tip/tilt/piston removal (bottom right).

In contrast to violations in the premise(s) of the measurement systems indicative of data outliers, the classification of spatial outliers in this work is primarily concerned with short-comings of the least-squares reconstruction algorithm. Again, consider the case of a shockwave: it is well known that shockwaves typically span space on the order of a few mean free paths of air, which can be considered a spatial discontinuity at the resolutions typical of SHWFS. That discontinuous nature should certainly be reflected in the solution. However, standard least-squares SHWFS reconstruction causes that sharpness to blur as the influence of the large residual due to the magnitude of the wavefront gradient at that location becomes large. In the bifurcated dot shown in Fig.2,

the effect of shockwaves not only violates the premise that the local wavefront gradient is determined purely via local tilt as in the case of a data outlier, the assumption that discontinuities should be "spatially coherent" in the reconstructed wavefront is also violated. The latter of these violations occur as a direct consequence of the reconstruction process.

2.2 Intensity Weighting Function

For this work, wavefront reconstruction algorithms were formulated and tested on SHWFS data acquired in Notre Dame's Mach 6 Hypersonic Quiet Tunnel. An example wavefront computed using the standard Southwell least-squares reconstruction method is shown in Fig.3, with flow moving from left to right. There was no model present in the tunnel test section, and the tunnel was not operating in its quiet configuration. As seen in the dot pattern, there exist multiple shockwaves that span the thickness of at least one lenslet. However, the least-squares reconstructed wavefront suggests a thicker shockwave structure. Additionally, the OPD before and after the shock are roughly the same value, suggesting that there is no change in density across the shock, which is non-physical. The non-physical nature of this result is due to the presence of both data and spatial outliers that standard SHWFS reconstruction methods are not able to account for.

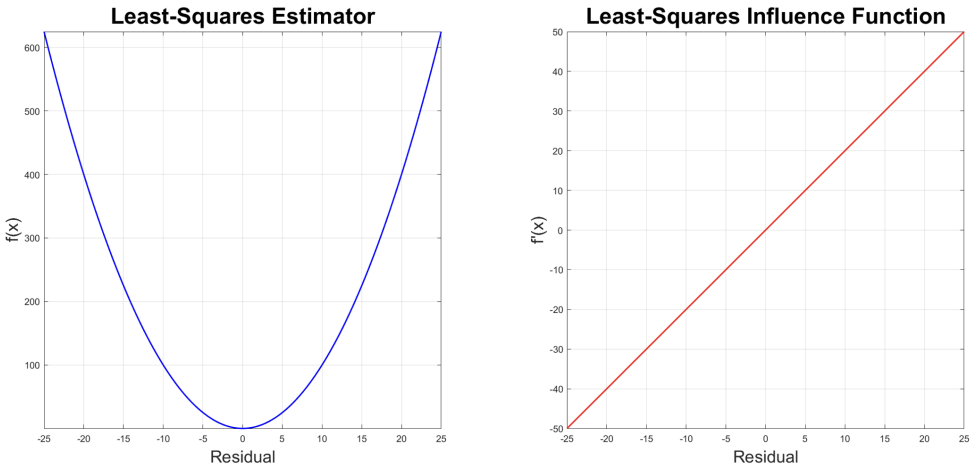

Figure 4. Quadratic estimator (left) with its corresponding influence function (right).

To address how outliers can be detected and handled, it is first important to establish the limitations of the least-squares method. A well-known shortcoming of least-squares estimation is the least-squares (quadratic) estimator's sensitivity to outliers. This sensitivity is illustrated in Fig.4, where the quadratic estimator is shown alongside its corresponding influence function. Specifically, the left plot of Fig.4 shows the magnitude of the term inside the integral of Eq. (4), while the right plot shows its derivative; hence Fig.4 right shows that the influence at any point in the solution domain linearly increases without bound as the magnitude of the residual increases. Large residual values at a point in the domain result in an over-contribution to the solution that negatively impacts the solution at other points in the domain. Therefore, the influence of outliers distributed among neighboring points results in a smoothing effect which violates the assumptions of spatial coherence imposed on the solution. These limitations inherent in least-squares wavefront reconstruction make improvements to the standard algorithm necessary. The goal is to reformulate Equation (5) to detect and handle outliers such that more accurate wavefront estimates can be recovered.

As previously mentioned, the focused intensity distribution within the lenslet AOIs no longer contains solely tilt effects when extreme flow phenomena are present. In other works,[9,14] heavily scintillated measurements lead to the appearance of branch points and branch cuts, which are "hidden" to SHWFS reconstruction, where an example from Steinbock et al.[14] is shown in Fig.5. This can lead to a broadening and diffusion of the dot that decrease the overall intensity, dot splitting in the case of dot bifurcation, or a combination of both. In order to represent these effects on the focused dots within the data, additional intensity information is required.

Two weighting functions were considered. The first looks at the overall illumination within each lenslet AOI and characterizes the change in illumination during flow-on conditions relative to some flow-off reference.

$$I_0 = \frac{1}{I_{norm} + \varepsilon}, \tag{7}$$

where I_{norm} is the sum of the intensity in the AOI normalized by a no-flow reference and ε is a small, non-negative value that prevents "blow-up" in cases where extreme turbulence leads to branch points that completely extinguish intensity in the AOI. In cases where extreme flow decreases the intensity within an AOI, I_0 takes on a value greater than unity, indicating that the slope of the wavefront at that measurement point is likely higher than what the SHWFS is capable of measuring. The advantage of Equation (7) is that it incorporates the effect of decreased intensity due to heavy scintillation, where intensity in the lenslet AOI may not be present at all or typical thresholding procedures may filter it out entirely.

In the case of dot bifurcation, significant decrease in intensity relative to some reference is not guaranteed, so additional intensity-based quantities are necessary. As detailed in Kalensky et al.,[15] the second-moment beam spread,

$$D4\sigma = 4\sqrt{\frac{\iint I(x,y,)(x-\overline{x})^2 dxdy}{\iint I(x,y)dxdy}}, \tag{8}$$

incorporates already-calculated information from the first central moment, calculated via Equation (3), where $D4\sigma$ is the 2nd moment beam spread, which has a direct relationship to the degree by which a focused beam is impacted by extreme variations in the OPD. From here, the second intensity-weighting function can be expressed as,

$$I_\sigma = \frac{D4\sigma_{flow} - D4\sigma_{ref}}{D4\sigma_{ref}}, \tag{9}$$

where the subscripts "ref" and "flow" indicate some reference (either no-flow or average) and flow-on measurements, respectively. Furthermore, since it can be observed that the intensity distributions in x and y exhibit

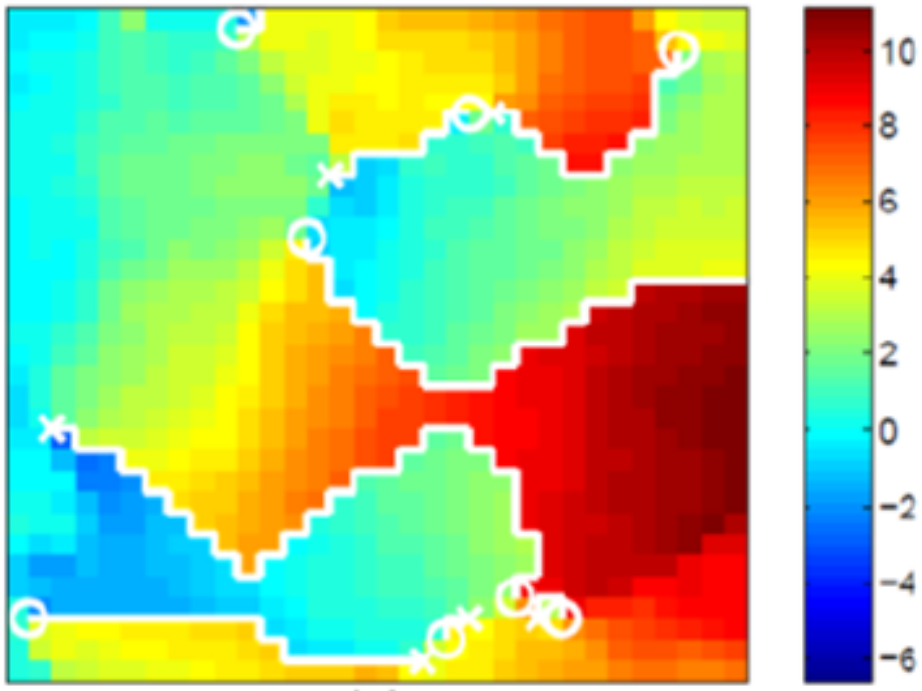

Figure 5. Phase map containing branch points (white circles) and branch cuts (white lines), from Steinbock et al.[14]

statistical independence, the $D4\sigma$ value in x and y can be individually applied to the corresponding local slope measurements. It should be noted that the incorporation of intensity information into the formulation is not dissimilar to the approach used in Kim et al.,[16] but the inclusion of $D4\sigma$ allows for additional information to be represented in the regression. For the intensity-weighting function, the reference-subtracted $D4\sigma$ value is used to characterize how much and in which direction(s) a dot is spreading due to extreme flow phenomena.

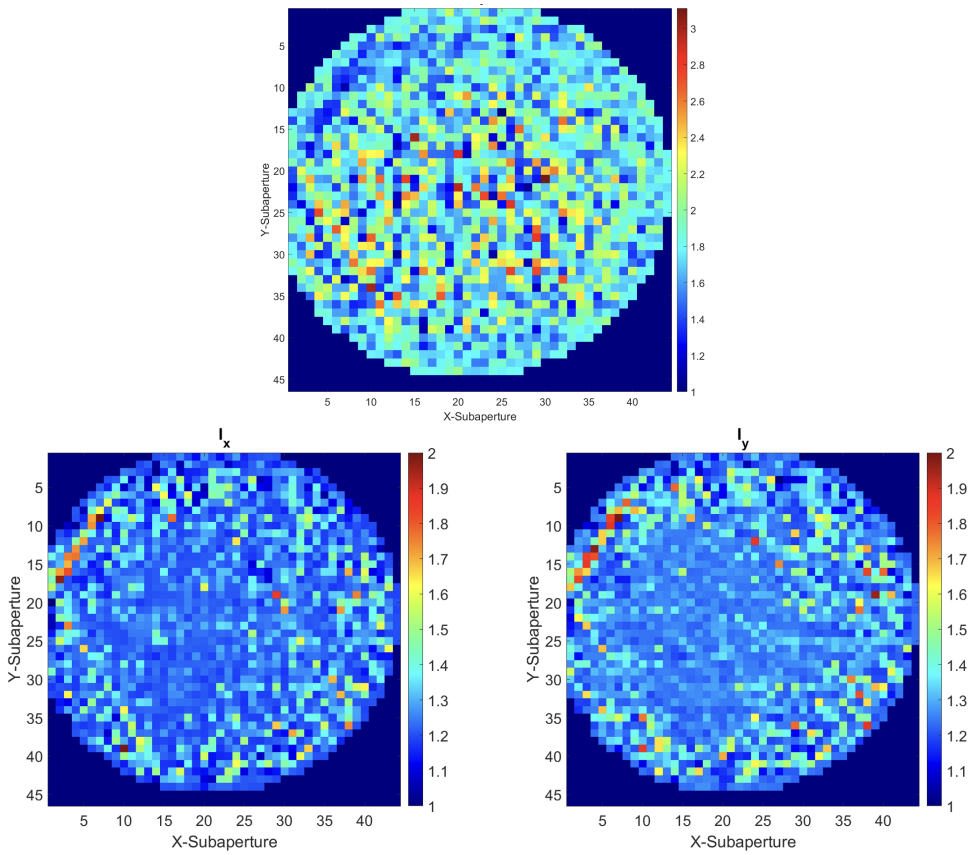

Figure 6. Intensity weighting function applied in both x and y directions based on overall intensity (top row) and second-moment beam spread (bottom row).

An example of these weighting functions is shown in Fig.6. Note that I_{norm} is non-directional, as the total intensity does not depend on the coordinate direction. As will be discussed later, the obvious presence of noise due to non-uniform illumination plays a significant role in the reconstruction. Still, the locations of the shocks are clearly represented in the weighting function. Recasting Equation (5) to include the intensity weights,

$$J(W) = \iint \|\nabla W - \theta^I\|_2^2 dxdy, \tag{10}$$

where the superscript indicates multiplication by an intensity-weighting function.

The intensity-weighted least-squares solution to wavefront reconstruction is shown in Figs.7 and 8, where it is compared to the standard least-squares approach. Close inspection reveals that the solution weighted by I_0 leads to an increase in OPD in the areas where shockwaves are expected in addition to increasing the overall OPD. In contrast, the solution weighted by I_σ has a relatively smaller increase in the same reconstruction locations. Furthermore, it may be seen from the absolute difference between the unweighted and weighted solutions that both weighting functions alter the solution around the oblique shocks, with I_0 leading to much larger magnitudes.

Perhaps the most convincing detail of Figures 8 and 9 is that the OPD magnitude experiences the most change after the shock, which is the expected result from the theoretical analysis and simulation results of Kalensky

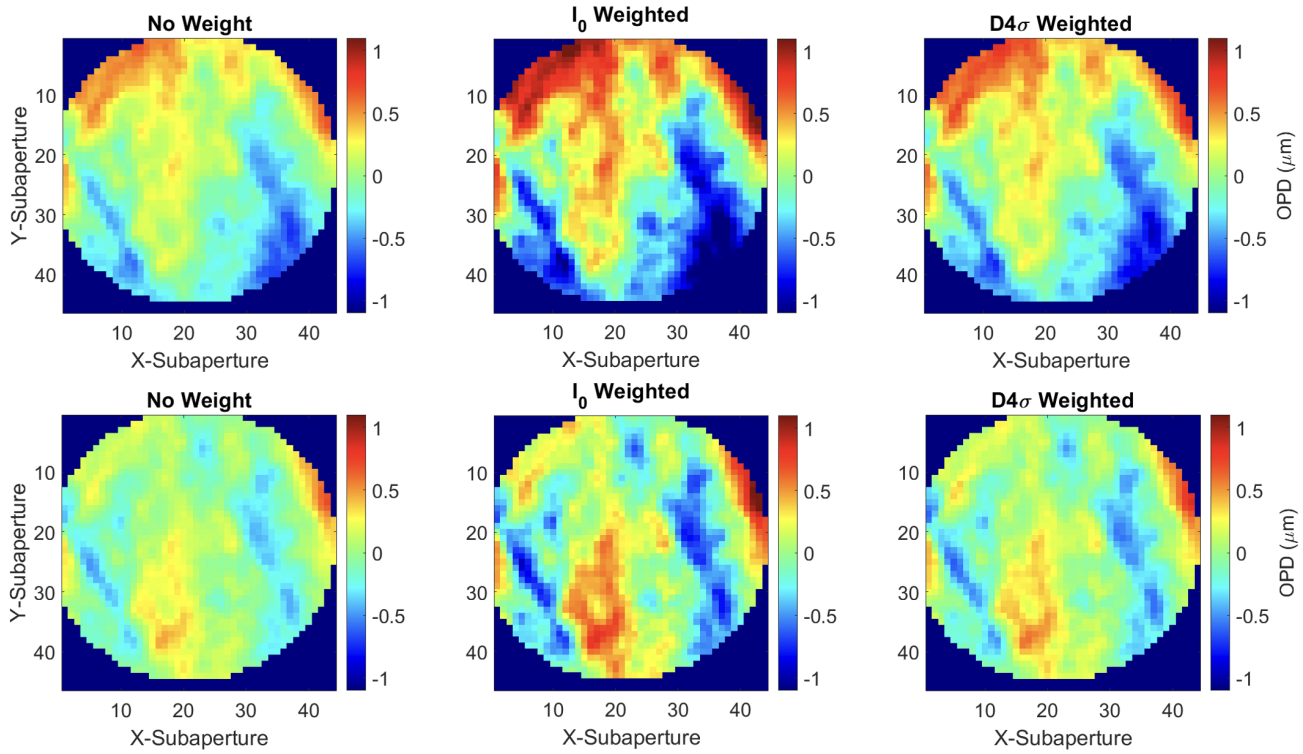

Figure 7. Comparison of unweighted least-squares reconstruction (left column) with overall intensity-weighted (middle column) and second-moment beam spread-weighted (right column) reconstructions, shown without (top row) and with (bottom row) tip/tilt/piston removed.

et al.[8] While promising, there still exists the issue of the spatial coherence of the shockwave. Specifically, the intensity-weighting function by itself does little to address the blurring of the shock into multiple domain points. In fact, because the slopes are artificially increased by the intensity weights, this contributes further to blurring as neighboring points are also influenced. The persistence of these spatial outliers highlights the need to develop more robust reconstruction algorithms.

3. ALGORITHM FORMULATION

3.1 Robust Estimation

As shown in Figures 8 and 9, to develop a robust formulation for wavefront reconstruction, the vulnerability of the least-squares (quadratic) estimator to the effects of outliers must be addressed. Whereas the intensity weighting function can be a necessary step to uncover outliers within the data, further reformulation provides the ability to reduce or remove the influence of those outliers on the solution. To overcome the problem of outlier sensitivity, the use of robust statistics is employed.

In computer vision research, the problem of outliers was addressed with robust M-estimators[17–20] in place of the least squares estimators typically employed. In applications such as denoising,[20] where the presence of noise can introduce large residual values, robust estimators can limit the influence that large residual values have on the overall solution, essentially preserving the underlying features. This idea was further extended to handle sharp gradients occurring in the data such as discontinuities.[21] This approach can also be used here to attenuate the influence of outliers on the overall solution.

A robust estimator can be chosen to replace the least squares estimator. For the current formulation, the Leclerc estimator was chosen,

$$f_L(x;c) = 1 - \exp\left[\frac{1}{2}\frac{x}{c}\right]^2, \tag{11}$$

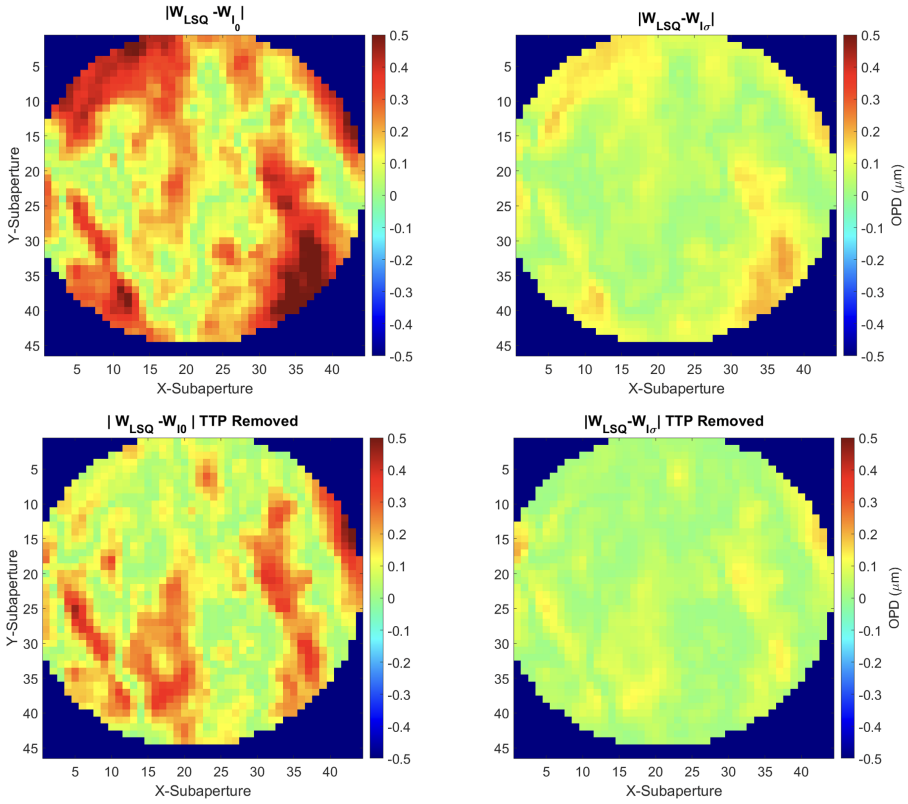

Figure 8. Absolute difference between unweighted least-squares and both overall intensity weighted least squares (left) and second-moment beam spread weighted least-squares (right).

where x is the residual and c is a tunable parameter that controls the width of the quadratic bowl near small residual values.

This estimator is chosen with two properties in mind: First the robust estimator is classified as a "redescending estimator," where the influence function of the estimator smoothly approaches zero for extreme outliers. Recall that, for the least-squares estimator, extreme outliers at one point in the domain will change the values at neighboring spatial points. This results in over-smoothing at locations where sharp gradients exist. The Leclerc estimator and its influence function are shown in Fig.9, where the decreasing value of the influence function for extreme residual values is a clear feature. Attenuating the influence of outliers allows for the preservation of sharp gradients that are typically observed in shockwaves.

The second property considered during estimator selection is the control parameter c. Fig.9 also shows the Leclerc estimator and its influence function plotted for different values of the control parameter, c. This parameter is key to determining what is considered an outlier, as increases in the control parameter value allow for larger values of residuals to be considered inliers, and vice versa. Measurements that exceed this threshold determined by c have their influence reduced. As such, the control parameter works as an outlier detection parameter that can be specified apriori, or even dynamically tuned during the iterative process.[22]

Unlike the quadratic estimator, redescending estimators are usually non-convex. This means that convergence to a global minimum is not guaranteed, making optimization tricky. To circumvent this limitation, it is possible to express Eq. 4 via an "outlier process",[22] at the cost of introducing a new minimizer for the objective functional. The outlier process allows Eq.4 to be expressed as a family of weighted quadratics, which can then be optimized in the least-squares sense while performing outlier rejection in the same way as a robust function. This makes convergence, at least theoretically, guaranteed. Minimization with respect to the outlier process would then be equivalent to minimization of the robust function with respect to its residual value and associated parameter

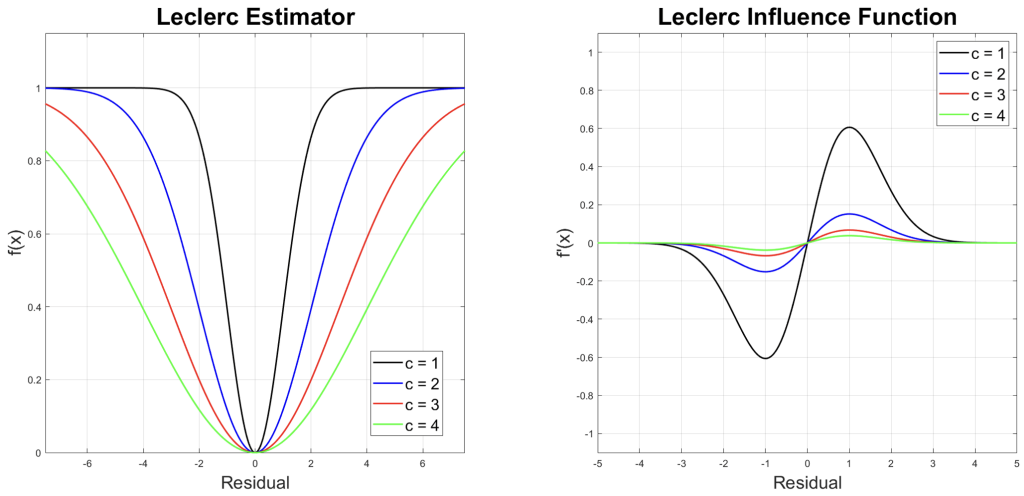

Figure 9. Leclerc estimator (left) and its corresponding influence function (right) for various values of the control parameter, c.

space.

The Leclerc estimator can be expressed as,

$$f_O(x, z; c) = \frac{1}{2} z \left[\frac{x}{c}\right]^2 + \psi(z), \tag{12}$$

where z is the outlier process introduced as a new minimizer to the functional and $\psi(z)$ is a convex and decreasing penalty function. Here, z takes values between 0 and 1 and $\psi(z)$ takes values from ∞ to 0. For the Leclerc estimator's penalty function we have,

$$\psi(z) = z \ln(z) - z + 1, \tag{13}$$

By inspection, when z approaches 1, there is no penalty imposed as the measurement is considered an inlier and the least-squares solution is preferred. When z approaches 0, the least-squares portion vanishes, and a heavy penalty is incurred for introducing an outlier. The outlier process z expresses the robust estimator as a family of quadratics that holds the advantage of convexity during optimization. Equation (12) for selected values of z is shown in Fig.10 to demonstrate this expression. Note that the reformulation retains the tunable control parameter c, which may still be used to control outlier detection thresholds.

3.2 Incorporating Regularizing Terms

While robust estimators are used here to perform outlier rejection, it is also necessary to explicitly include additional constraints on the spatial organization of the data within the objective functional. For the current formulation, two regularizing terms are considered. First, recall that outliers present in the data consist of erroneously calculated centroids. Measurements of scintillated or bifurcated dots not only produce unreliable centroids, but also lead to unreliably calculated slopes. Recall the strong formulation presented in Equation (6), where the slope divergence is equated with the wavefront Laplacian; with the intensity weighting functions from Equation (7) and Equation (9), the divergence of the weighted slopes may cause solution divergence during the iterative process. Therefore, the spatial coherence of the wavefront must be explicitly enforced. As the current formulation already consists of a constraint applied to the wavefront gradient, adding a regularizing term that constrains the wavefront Laplacian itself is considered. This leads to the new global energy functional,

$$J(W) = \iint f_0\left(\|\nabla W - \theta\|_2; c_d\right) dxdy + \alpha^2 \iint f_0\left(\|\nabla^2 W\|_2; c_s\right) dxdy, \tag{14}$$

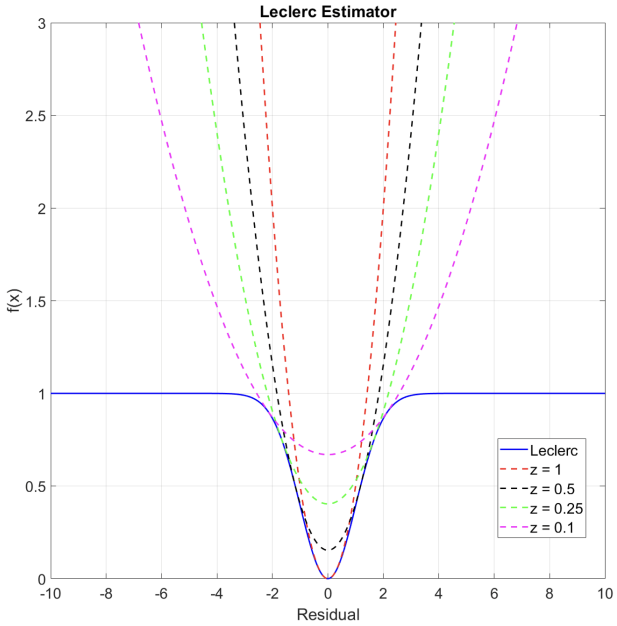

Figure 10. Leclerc estimator and its family of quadratics, shown for various values of the outlier process, z.

where the first term is a measure of "data fidelity" (subscript d); the solution's adherence to measured data, the second term is a constraint placed on the spatial coherence of the solution (subscript s), and α is the regularization parameter that balances the relative importance between the two terms. Here, both the data fidelity and spatial coherence terms are estimated with the Leclerc function. This formulation is similar to that of Bardsley,[23,24] with the exception that robust M-estimators are used to replace the least-squares estimators. Bardsley[23] theoretically proved that the solution to Equation (14) forms a well-posed system that strongly converges to a unique solution when the estimator f_0 is quadratic. The second regularizing term considered seeks to preserve the spatial characteristics of the least-squares solution, which is known to be accurate at locations absent of outliers. In order to do this, the inclusion of the least-squares reconstructed wavefront as a prior is necessary. Specifically, minimizing the difference between the robust reconstruction and the least-squares reconstruction can be expressed as,

$$\beta^2 \iint \left(W - W_{LSQ}\right)^2 dxdy, \tag{15}$$

where W_{LSQ} is the least-squares estimation of the wavefront and β is the regularization parameter that balances the importance of this term with the data term and the spatial coherence term. This coercive, zeroth-order regularizing term forces the reconstruction to comply with the least-squares estimates where the least-squares estimates are assumed to be accurate—where there is little to no scintillation or dot bifurcation and therefore no gross outliers. The new global energy functional can be expressed as,

$$J\left(W\right) = \iint f_0\left(\|\nabla W - \theta\|_2; c_d\right) dxdy + \alpha^2 \iint f_0\left(\|\nabla^2 W\|_2; c_s\right) dxdy + \beta^2 \iint \left(W - W_{LSQ}\right)^2 dxdy, \tag{16}$$

The Euler-Lagrange Equations are again used to solve this system. For minimization with respect to the wavefront value W,

$$2\beta^2\left(W - W_{LSQ}\right) = \frac{2}{c_d^2}\left[\nabla z_d \cdot \nabla W^I - \nabla z_d \cdot \theta^I + z_d \nabla^2 W^I - z_d \nabla \cdot \theta\right] - \frac{2\alpha^2}{c_s^2}\left[\nabla^2 z_s \nabla^2 W + z_s \nabla^4 W\right]. \tag{17}$$

Note that even though the representation of the robust M-estimators requires the introduction of additional minimizers to the objective functional, the penalty functions are only functions of their respective outlier process,z,

and expressions for the optimal outlier process values are known in closed form. For the Leclerc penalty function we have,

$$z_d = \exp\left[-\frac{\|\nabla W - \theta\|_2^2}{2c_d^2}\right], \tag{18}$$

$$z_s = \exp\left[-\frac{\left(\nabla^2 W\right)^2}{2c_s^2}\right], \tag{19}$$

which depends solely on their respective residual values. For minimization with respect to the wavefront estimate, W, the optimality conditions in Equation (16) yield a biharmonic equation which can be solved using finite differences to approximate the continuous differential operators. The approximations come in the form of kernels that are convolved with their corresponding quantities to yield approximations of derivatives at some central point (i, j) for which the Laplacian and biharmonic operators have a non-zero value. As convolution is a distributive process, the discrete derivative operators can be separated, and the convolution can be performed as a linear combination of two convolutions. The Laplacian can be approximated as convolution with the separable kernel, K_L,

$$K_L = \begin{bmatrix} 0 & 1 & 0 \\ 1 & -4 & 1 \\ 0 & 1 & 0 \end{bmatrix} = \begin{bmatrix} 0 & 1 & 0 \\ 1 & 0 & 1 \\ 0 & 1 & 0 \end{bmatrix} + \begin{bmatrix} 0 & 0 & 0 \\ 0 & -4 & 0 \\ 0 & 0 & 0 \end{bmatrix}. \tag{20}$$

Similarly, the discrete Biharmonic can be expressed as,

$$K_H = \begin{bmatrix} 0 & 0 & 1 & 0 & 0 \\ 0 & 2 & -8 & 2 & 0 \\ 1 & -8 & 20 & -8 & 1 \\ 0 & 2 & -8 & 2 & 0 \\ 0 & 0 & 1 & 0 & 0 \end{bmatrix} = \begin{bmatrix} 0 & 0 & 1 & 0 & 0 \\ 0 & 2 & -8 & 2 & 0 \\ 1 & -8 & 0 & -8 & 1 \\ 0 & 2 & -8 & 2 & 0 \\ 0 & 0 & 1 & 0 & 0 \end{bmatrix} + \begin{bmatrix} 0 & 0 & 0 & 0 & 0 \\ 0 & 0 & 0 & 0 & 0 \\ 0 & 0 & 20 & 0 & 0 \\ 0 & 0 & 0 & 0 & 0 \\ 0 & 0 & 0 & 0 & 0 \end{bmatrix}. \tag{21}$$

Note that the values surrounding the central point of the discrete Laplacian and Biharmonic operators can be regarded as a first and second-order neighborhood average of points, respectively. For the Biharmonic operator, it is apparent that the effect of incorporating spatial information beyond the limits of the first-order neighborhood allows for the algorithm to better determine acceptable values of the wavefront that abide by the constraints encoded within the objective functional. By substituting Equation (20) and Equation (21) into Equation (17) and separating all terms containing the central point we have,

$$W(i,j) = \frac{\frac{1}{c_d^2}\left[\nabla z_d \cdot \nabla W^I - \nabla z_d \cdot \theta^I + 4 z_d \overline{W}_L^I - z_d \nabla \cdot \theta^I\right] + \frac{\alpha^2}{c_s^2}\left[4\nabla^2 z_s \overline{W}_L - 20 z_s \overline{W}_H\right] + \beta^2 W_{LSQ}}{\left[\beta^2 + \frac{4 z_d^I}{c_d^2} - \frac{4\alpha^2 \nabla^2 z_s}{c_s^2} + \frac{20\alpha^2 z_s}{c_s^2}\right]}, \tag{22}$$

where the overbars denote spatial averaging, and the subscripts L and H indicate the Laplacian (first-order) and Biharmonic (second-order) spatial neighborhoods, respectively. The left-hand side of Equation (22) denotes the current iteration, calculated by the previous iteration on the right-hand side.

4. PARAMETER OPTIMIZATION

4.1 Outlier Detection Parameters

Inspecting the outlier process equations, it is obvious to see the role that the outlier detection parameter plays in determining what residual values present in the domain constitute outliers and to what extent. However, specifying the control parameter values that accurately detect outliers can be tricky. In general, the control parameter c can be initially fixed such that the robust estimation treats all points in the domain as fixed. The value at which this occurs can be obtained from the second derivative test of the chosen estimator. When the second derivative is positive, the convexity condition is satisfied,

$$\frac{\partial^2}{\partial x^2} f_L(x; c) > 0, \tag{23}$$

where x, in this case, is the value of the residual at a point. For the Leclerc function, convexity is achieved for all points in the domain if and only if,

$$c_{convex} \geq \sqrt{2} \max\left(|x|\right), \tag{24}$$

As in Black and Rangarangan,[22] parameter continuation schemes may be employed to iteratively decrease the initially set value of the outlier detection parameter, which in turn would slowly uncover outliers and handle them according to the properties of the chosen robust estimator(s).

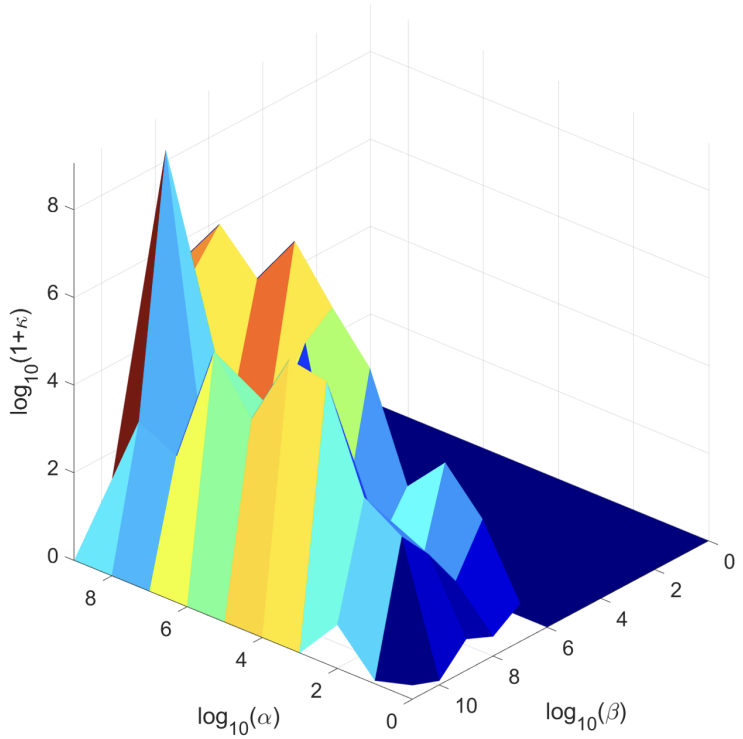

Figure 11. L-Hypersurface Gaussian Curvature for both weighting functions. Peak Gaussian Curvature occurs at 10^8 and 10^9 for β and α, respectively.

Although the parameter continuation method can be used for the current algorithm, there exists enough knowledge about the physical measurement system to seek out a constant parameter in the case of SHWFS measurements. For the data term, an outlier threshold may be directly derived as the maximum slope that is measurable by a given AOI in a SHWFS,

$$\theta_{max} = \frac{\delta_L}{2f_L} - \frac{2\lambda}{\delta_L}, \tag{25}$$

where δ_L is the lenslet pitch and λ is the wavelength of the laser source. The second term on the right of Equation (25) is the diffraction-limited spot size for a Gaussian beam; hence Equation (25) gives the maximum local slope for which the spot stays within the boundaries of a given AOI. From here, the maximum measurable wavefront Laplacian can be assumed to equal the maximum measurable slope divergence and may similarly be expressed using central difference approximations as,

$$\nabla^2 W_{max} = (\nabla \cdot \theta)_{max} = \frac{1}{2f_L} - \frac{\lambda}{2\delta_L^2}, \tag{26}$$

The significance of the intensity weighting functions is also seen here; for AOIs that contain scintillated or bifurcated dots, the first central moment would never exceed the limit presented in Equation (25). Artificially increasing the slope measurements would allow for the threshold to be exceeded, and therefore detected as a

data outlier. Slope measurements that exceed the lenslet measurement range may then give rise to wavefront Laplacian values that exceed the limit specified in Equation (26), which would in turn be detected as a spatial outlier.

4.2 Regularization Parameters

As previously stated, the regularization parameters balance the relative importance of each term. For the case of only one regularizing term, plotting the residual of the data term versus the residual of the regularizing term for multiple regularization parameter values yields a curve that, in many cases, has a shape that resembles an L (see Hansen,[25] Figure 2). The optimal regularization parameter exists at the "corner" of this L-curve, and that corner is the point of maximum curvature, again parameterized by the regularization parameter value. From Belge et al.,[26] this method was generalized to include multiple regularization parameters, where the optimal set of regularization parameters exist at the point where the Gaussian Curvature of the now L-hypersurface is maximized. Opting for the grid-search method instead of the iterative method developed in Belge et al.,[26] the L-hypersurface is presented in Fig.11. The optimal regularization parameters were on the order of 10^8 and 10^9 for β and α, respectively. While seemingly large, the magnitudes of the parameters are necessary to balance errors in the data and regularizing terms.

5. RESULTS AND DISCUSSION

The algorithm was tested on a sample dot pattern from SHWFS data acquired in the University of Notre Dame's Mach 6 Quiet Tunnel. For this run, the total temperature, T0, was recorded at 455.37K, the total pressure, P0, was recorded at 655kPa, and the back pressure, Pb, was recorded at 1.5kPa. More information on the specifications of the Mach 6 Quiet Tunnel can be found in Lakebrink et al.[27] The lenslet array had a pitch of 0.0003m and a focal length of 0.0382m. Intensity-weighted slopes for both weighting functions are shown alongside the unweighted slopes in Fig.12. It is clear to see where the shocks occur, as the intensity-weighted slopes take larger values than the unweighted slopes in the same areas that contain heavily scintillated or bifurcated dots. In the case of the slopes weighted by the overall intensity, the overall magnitude of the slopes is increased, while only some isolated effects around the shock regions. On the other hand, slopes weighted by second moment beam spread have a better ability to solely target the shock regions.

The outlier processes for the data term and the spatial term for both weighting functions are shown in Fig.13. Recall that, for residual values close to unity, there is little to no penalty incurred and the estimator influence approaches that of a least-squares estimator. As can be seen from the data outlier process using the overall intensity weight, the shocks are correctly targeted, taking values relatively less than unity. However, due to the non-uniform illumination, the calculated intensity weights are very noisy, which may be the cause of the much thicker data outlier detection around the shock locations in this case. For the data outlier processes weighted by the second-moment beam spread, the detected data outliers more precisely target only the shocks. Although the second-moment intensity weighting function is still noisy, it is relatively less noisy than the overall intensity weighting function, which may contribute to that precision. In both cases, the spatial outlier process shows little to no deviation from unity. It should be noted that this doesn't necessarily mean that there are no spatial outliers in the solution, but that the robust functions did not detect any outliers. This may be traced back to the specification of the outlier threshold from Equation (26), where further work is needed to ensure that the threshold is properly specified. In this case, parameter continuation can be applied, where the value of cs is incrementally decreased until spatial outliers are detected, but that is to be explored in future work.

The reconstructed wavefront for both weighting functions are shown in Fig.14. It can be seen that the regions where shocks are expected qualitatively have a much sharper appearance in the robust reconstruction than in the least-squares reconstruction. More concrete evidence of this can be seen in Fig.15, where horizontal and vertical slices are plotted to compare both weighting functions' ability to retain the sharp resolution typically associated with shockwaves. In areas where the shock is expected to occur, the robust reconstruction shows more resolute peaks with a much sharper gradient. Perhaps most promising is the difference in OPD around the shock locations; in both cases, the robust reconstruction produces higher absolute values of OPD around the shock locations, which is the theoretically expected result.[8]

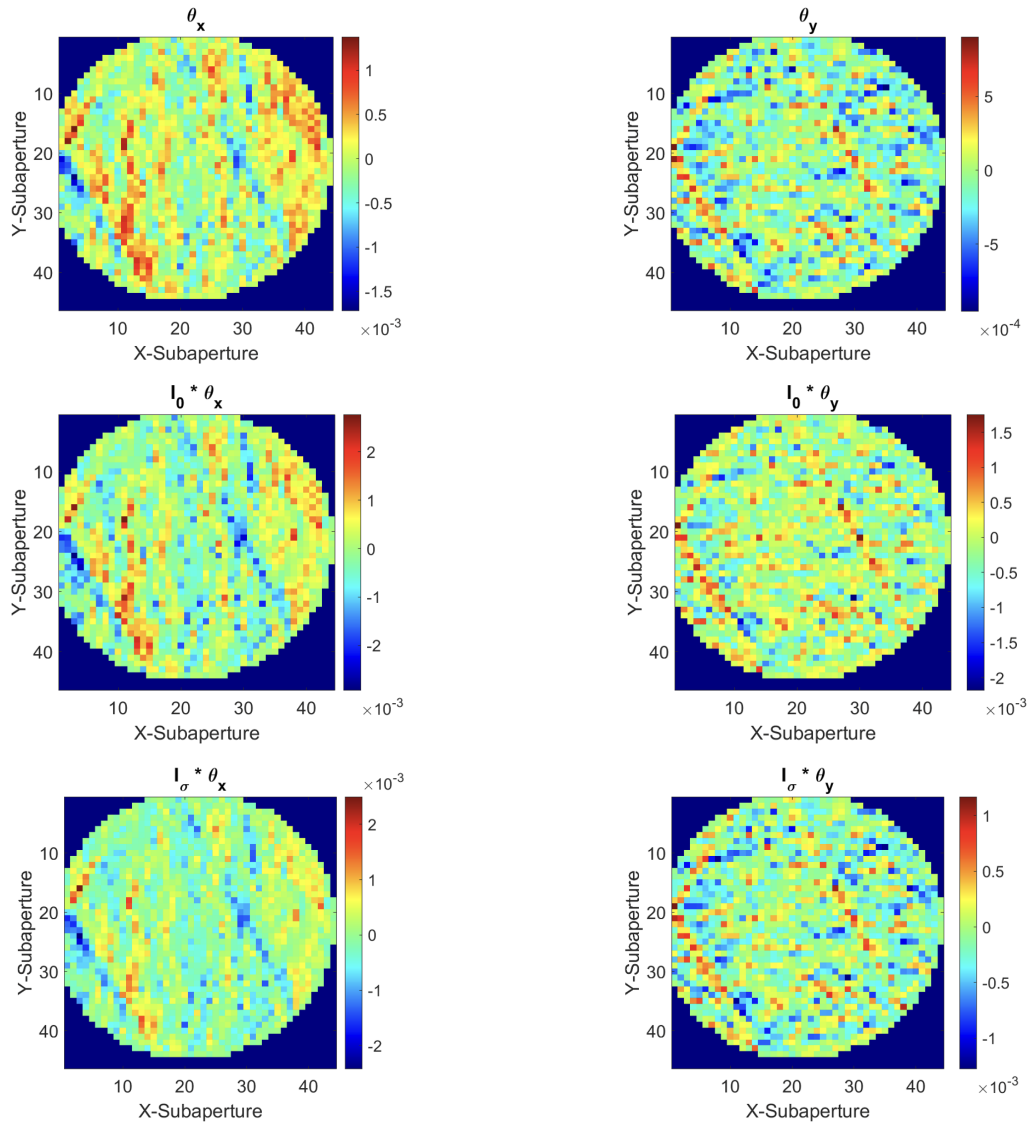

Figure 12. Comparison of unweighted slopes (top row) and intensity-weighted X and Y slopes for both overall intensity weighting (middle row) and second-moment beam spread weighting (bottom row).

6. CONCLUSION

The problem of aero-optic wavefront reconstruction from SHWFS dot patterns in the presence of discontinuities such as shocks was investigated. By taking a closer look at the effect that extreme flow phenomena have on the intensity distribution within a lenslet AOI, it becomes clear that the assumption of tilt-only behavior within the AOI is violated for significant enough changes in OPD. The standard reconstruction method's utilization of the first-central moment leads to slope values that are not accurately representative of the true change in OPD across the AOI, which leads to a loss of accuracy of the reconstructed wavefront. To address this loss of accuracy, it is necessary to incorporate additional statistical information from the lenslet AOI intensity distribution. As such, two intensity weighting functions were formulated with the intent of encoding the effect of scintillation and bifurcation into the reconstruction algorithm. The first of these functions is based on the total intensity within a lenslet AOI, which considers the tendency of extreme flow phenomena to decrease the illumination within an AOI. The second intensity weighting function is based on the second-moment beam spread, which has a more

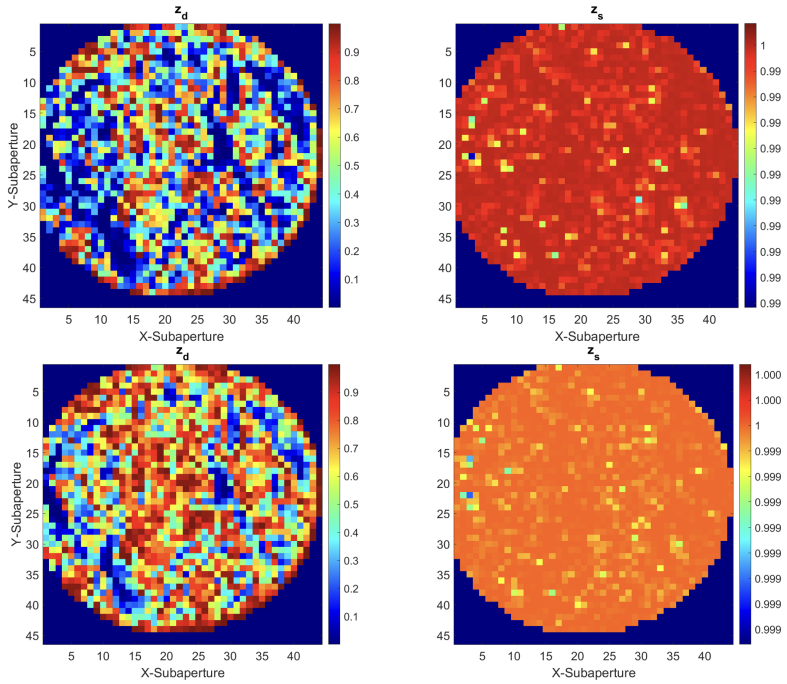

Figure 13. Data outlier process (left column) and spatial outlier process (right column) for both overall intensity weighting (top row) and second-moment beam spread weighting (bottom row).

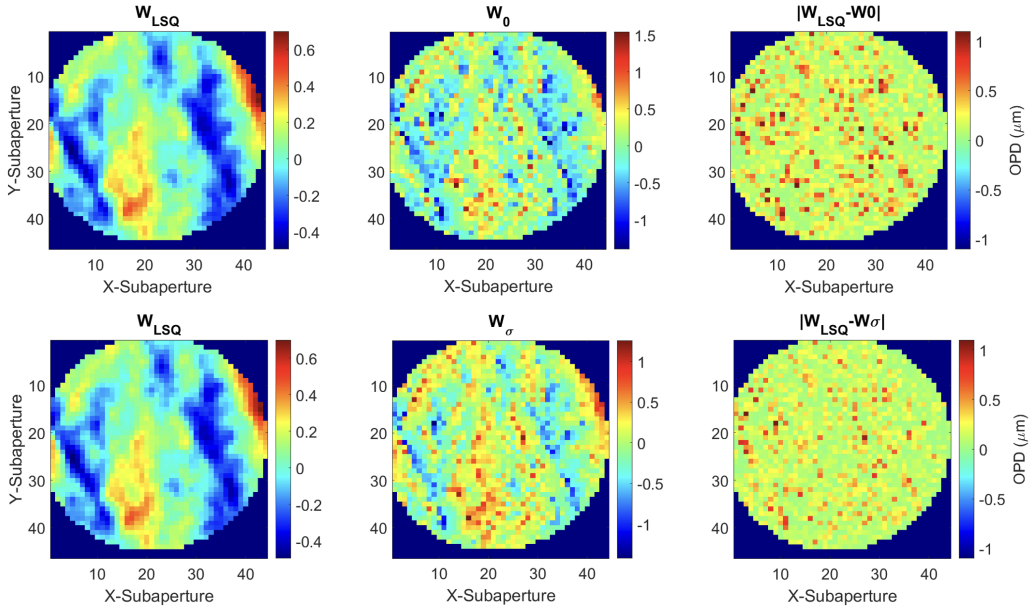

Figure 14. Reconstructed wavefront using Mach 6 Quiet Tunnel Data. A comparison is shown for both the overall intensity weighting (top row) and second-moment beam intensity weighting (bottom row). The least-squares (left column) shows smaller peak OPD magnitudes than the robust (middle column). The absolute difference (right column) shows that the areas surrounding the shockwaves experience the most change in OPD.

concrete statistical relationship to the change in OPD within an AOI. Weighting the least-squares reconstruction with either intensity weight leads to an overall increase in the OPD in the areas that contain shockwaves but does nothing to address the thick shock structure that is not observed in the raw data. This effect in the data was

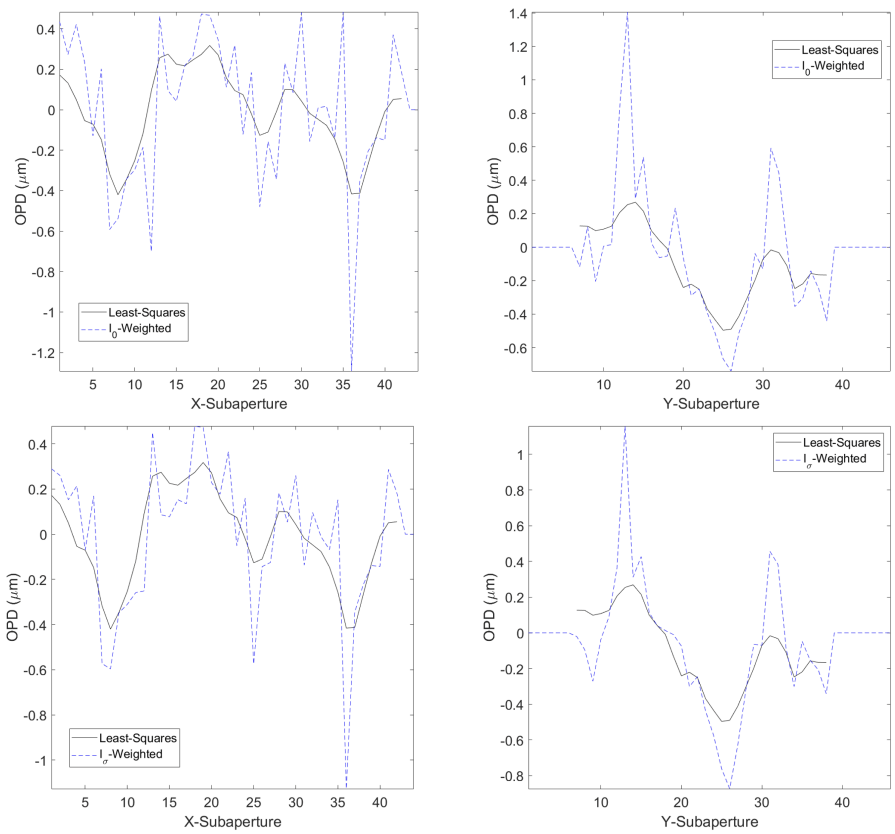

Figure 15. 1D Slices in both x-direction (left column) taken at the 30th y-lenslet and y-direction (right column) taken at the 5th x-lenslet for both overall intensity weighting (top row) and second-moment beam weighting (bottom row).

shown to be caused by the quadratic estimator, resulting in a "smoothing effect" around the sharp gradients of the shockwave. This problem was exacerbated by the intensity weighting functions, which artificially increased the slope measurements in those regions.

In order to address the short-comings of the standard SHWFS reconstruction algorithm, the quadratic estimator was replaced by robust, non-convex M-estimators, which have the advantage of reducing the influence of outliers over the rest of the solution. The Leclerc function was chosen for its ability to attenuate the influence of extreme outliers to have no influence over the solution, preserving sharp gradients in areas where they exist. By expressing the Leclerc estimator as a family of quadratics via the outlier process method, solution convergence was guaranteed at the cost of introducing the outlier process as a new variable to minimize in the reconstruction.

In addition to the Leclerc estimator, two regularizing terms were added to assist in constraining the solution. Both a spatial coherence constraint on the Laplacian of the wavefront and a 0th order coercive constraint were added, yielding a global energy functional. Minimization was performed using the Euler-Lagrange method, producing a biharmonic equation. Finite differences were then used to produce an iterative solution. The L-hypersurface scheme was adopted as a sub-optimization routine to uncover the perfect set of regularization parameters, while the physical measurement system was used to determine outlier detection thresholds.

The robust reconstruction for both intensity weighting functions was compared to the least-squares reconstruction. It can be seen from the results that the robust reconstruction properly identified the oblique shocks as outliers for both intensity weighting functions, which resulted in greatly improved resolution around the shock. Selected horizontal and vertical slices of the wavefront revealed significantly increased OPD at the locations where shocks occur, more so for the intensity weighting function based on the overall intensity. The outlier processes for both weighting functions tells a similar story, with the outlier process based on the second-moment

beam spread having a more precise outlier detection of shocks than that of the overall intensity. While the results clearly demonstrate the algorithm's ability to target and handle outliers on real data, it is still unclear if the reconstructed wavefront is a more accurate representation of the true OPD than the least-squares reconstruction. A proper analysis of this can be done using a simulated wavefront discontinuity with known phase. It is also unknown if the choice of estimator or outlier detection parameter threshold was adequate to accurately capture outliers. This is in-part due to the non-uniform illumination, which led to noise in the intensity weighting functions. These questions are currently being explored for future works.

DISCLOSURES

The views expressed are those of the author and do not necessarily reflect the official policy or position of the Department of the Air Force, the Department of Defense, or the U.S. government. Approved for public release; distribution is unlimited. Public Affairs release approval #AFRL-2023-4755.

ACKNOWLEDGMENTS

The authors would like to acknowledge Aaron Fassler for his contribution of the dataset from the Whitefield Mach 6 Quiet Tunnel.

REFERENCES

[1] Jumper, E. J. and Gordeyev, S., "Physics and measurement of aero-optical effects: Past and present," *Annual Review of Fluid Mechanics* **49**(1), 419–441 (2017).

[2] Duffin, D. A. and Jumper, E. J., "Feedforward adaptive-optic correction of aero-optical aberrations caused by a two-dimensional heated jet," *AIAA Journal* **49**(6), 1283–1291 (2011).

[3] Gordeyev, S. and Jumper, E., "Fluid dynamics and aero-optics of turrets," *Progress in Aerospace Sciences* **46**(8), 388–400 (2010).

[4] Spencer, M. F., "Limitations of the deep-turbulence problem," in [*OSA Imaging and Applied Optics Congress 2021 (3D, COSI, DH, ISA, pcAOP)*], *OSA Imaging and Applied Optics Congress 2021 (3D, COSI, DH, ISA, pcAOP)* , PW3F.1, Optica Publishing Group (2021).

[5] Steinbock, M. J., Hyde, M. W., and Schmidt, J. D., "Lspv+7, a branch-point-tolerant reconstructor for strong turbulence adaptive optics," *Appl. Opt.* **53**, 3821–3831 (Jun 2014).

[6] Murphy, K., Burke, D., Devaney, N., and Dainty, C., "Experimental detection of optical vortices with a shack-hartmann wavefront sensor," *Opt. Express* **18**, 15448–15460 (Jul 2010).

[7] Kalensky, M., Kemnetz, M. R., and Spencer, M. F., "Effects of shock waves on shack–hartmann wavefront sensor data," *AIAA Journal* **61**(6), 2356–2368 (2023).

[8] Kalensky, M., Kemnetz, M. R., and Spencer, M. F., "Effects of shock-related discontinuities on SHWFS measurements: modeling and simulation," in [*Unconventional Imaging and Adaptive Optics 2022*], Dolne, J. J. and Spencer, M. F., eds., **12239**, 122390J, International Society for Optics and Photonics, SPIE (2022).

[9] Watnik, A. T. and Gardner, D. F., "Wavefront sensing in deep turbulence," *Optics and Photonics News* **29**(10), 38–45 (2018).

[10] Hudgin, R. H., "Wave-front reconstruction for compensated imaging," *J. Opt. Soc. Am.* **67**, 375–378 (Mar 1977).

[11] Fried, D. L., "Least-square fitting a wave-front distortion estimate to an array of phase-difference measurements," *J. Opt. Soc. Am.* **67**, 370–375 (Mar 1977).

[12] Southwell, W., "Wave-front estimation from wave-front slope measurements," *J. Opt. Soc. Am.* **70**, 998–1006 (Aug 1980).

[13] Li, S. Z., Wang, H., and Soh, W. Y., "Robust estimation of rotation angles from image sequences using the annealing m-estimator," *Journal of Mathematical Imaging and Vision* **8**, 181–192 (Mar 1998).

[14] Steinbock, M. J., Schmidt, J. D., and Hyde, M. W., "Comparison of branch point tolerant wavefront reconstructors in the presence of simulated noise effects," in [*2012 IEEE Aerospace Conference*], 1–13 (2012).

[15] Kalensky, M., "Branch-point identification using second-moment shack–hartmann wavefront sensor statistics," *Appl. Opt.* **62**, G101–G111 (Aug 2023).

[16] Kim, J. J., Fernandez, B., and Agrawal, B., "Iterative wavefront reconstruction for strong turbulence using shack–hartmann wavefront sensor measurements," *J. Opt. Soc. Am. A* **38**, 456–464 (Mar 2021).

[17] Chan, R. H. and Liang, H.-X., "Half-quadratic algorithm for $l_p - l_q$ problems with applications to tv-l_1 image restoration and compressive sensing," in [*Efficient Algorithms for Global Optimization Methods in Computer Vision*], Bruhn, A., Pock, T., and Tai, X.-C., eds., 78–103, Springer Berlin Heidelberg, Berlin, Heidelberg (2014).

[18] Bilgic, B., Chatnuntawech, I., Fan, A. P., Setsompop, K., Cauley, S. F., Wald, L. L., and Adalsteinsson, E., "Fast image reconstruction with l2-regularization," *Journal of Magnetic Resonance Imaging* **40**(1), 181–191 (2014).

[19] Weickert, J. and Schnörr, C., "A theoretical framework for convex regularizers in pde-based computation of image motion," *International Journal of Computer Vision* **45**, 245–264 (Dec 2001).

[20] Nikolova, M., Ng, M. K., and Tam, C.-P., "On l_1 data fitting and concave regularization for image recovery," *SIAM Journal on Scientific Computing* **35**(1), A397–A430 (2013).

[21] Monzón, N., Salgado, A., and Sánchez, J., "Regularization strategies for discontinuity-preserving optical flow methods," *IEEE Transactions on Image Processing* **25**(4), 1580–1591 (2016).

[22] Black, M. J. and Rangarajan, A., "On the unification of line processes, outlier rejection, and robust statistics with applications in early vision," *International Journal of Computer Vision* **19**, 57–91 (Jul 1996).

[23] Bardsley, J. M., "An analysis of methods for wavefront reconstruction from gradient measurements in adaptive optics,"

[24] Bardsley, J. M., "Wavefront reconstruction methods for adaptive optics systems on ground-based telescopes," *SIAM Journal on Matrix Analysis and Applications* **30**(1), 67–83 (2008).

[25] Hansen, P., "The l-curve and its use in the numerical treatment of inverse problems," in [*InviteComputational Inverse Problems in Electrocardiology*], WIT Press (2000). InviteComputational Inverse Problems in Electrocardiology ; Conference date: 01-01-2000.

[26] Belge, M., Kilmer, M. E., and Miller, E. L., "Efficient determination of multiple regularization parameters in a generalized l-curve framework," *Inverse Problems* **18**, 1161 (jul 2002).

[27] Lakebrink, M. T., Bowcutt, K. G., Winfree, T., Huffman, C. C., and Juliano, T. J., "Optimization of a mach-6 quiet wind-tunnel nozzle," *Journal of Spacecraft and Rockets* **55**(2), 315–321 (2018).